# Dual-functional β-$NaYF_4$: $Yb^{3+}$, $Er^{3+}$ nanoparticles for bioimaging and temperature sensing

**Lili Huo,[1] Jiajia Zhou,[1,2] Ruozhen Wu,[1] Junfei Ren,[1] Shengjun Zhang,[1] Junjie Zhang,[1] and Shiqing Xu[1,3]**

[1]*College of Materials Science and Engineering, China Jiliang University, Hangzhou 310018, China*
[2]*zhzz85@zju.edu.cn*
[3]*Shiqingxu@c-jlu.edu.cn*

**Abstract:** Hexagonal-phase $NaYF_4$: $Yb^{3+}$, $Er^{3+}$ nanoparticles (NPs) have been widely used as the most efficient NIR-to-visible upconversion (UC) luminescent and probe in bioscience. Here, we exploited not only the function of dual-mode emission of β-$NaYF_4$: $Yb^{3+}$, $Er^{3+}$ NPs in the near infrared (NIR) and visible regions with single wavelength excitation at 980 nm, but also the function of physiological temperature sensing with the luminescence of $Er^{3+}$ in the visible region. The structural and optical characteristics of β-$NaYF_4$: $Yb^{3+}$, $Er^{3+}$ NPs were obtained using X-ray diffraction (XRD), scanning electron microscopy (SEM),and fluorescence spectral measurements, respectively; the mechanism for the energy transfer has been suggested with emphasis on the optimized Er/Yb concentration for most efficient UC. Due to the UC and down-shifting NIR properties, we achieved the dual-functional nanoparticles with potential application in physiological range temperature sensing and bioimaging simultaneously.



**OCIS codes:** (160.2540) Fluorescent and luminescent materials; (300.6340) Spectroscopy, infrared; (160.5690) Rare-earth-doped materials.

## References and links

1. R. Wang and F. Zhang, "NIR luminescent nanomaterials for biomedical imaging," J. Mater. Chem. B Mater. Biol. Med. **2**(17), 2422–2443 (2014).
2. S. Adams, R. P. Baum, T. Stuckensen, K. Bitter, and G. Hör, "Prospective comparison of 18F-FDG PET with conventional imaging modalities (CT, MRI, US) in lymph node staging of head and neck cancer," Eur. J. Nucl. Med. **25**(9), 1255–1260 (1998).
3. G. Hong, J. T. Robinson, Y. Zhang, S. Diao, A. L. Antaris, Q. Wang, and H. Dai, "In vivo fluorescence imaging with $Ag_2S$ quantum dots in the second near-infrared region," Angew. Chem. Int. Ed. Engl. **51**(39), 9818–9821 (2012).
4. R. Weissleder, "A clearer vision for in vivo imaging," Nat. Biotechnol. **19**(4), 316–317 (2001).
5. V. Pansare, S. Hejazi, W. Faenza, and R. K. Prud'homme, "Review of long-wavelength optical and NIR imaging materials: contrast agents, fluorophores, and multifunctional nano carriers," Chem. Mater. **24**(5), 812–827 (2012).
6. J. V. Frangioni, "In vivo near-infrared fluorescence imaging," Curr. Opin. Chem. Biol. **7**(5), 626–634 (2003).
7. D. J. Naczynski, M. C. Tan, M. Zevon, B. Wall, J. Kohl, A. Kulesa, S. Chen, C. M. Roth, R. E. Riman, and P. V. Moghe, "Rare-earth-doped biological composites as in vivo shortwave infrared reporters," Nat. Commun. **4**, 2199 (2013).
8. Y. Yang, Q. Shao, R. Deng, C. Wang, X. Teng, K. Cheng, Z. Cheng, L. Huang, Z. Liu, X. Liu, and B. Xing, "In vitro and in vivo uncaging and bioluminescence imaging by using photocaged upconversion nanoparticles," Angew. Chem. Int. Ed. Engl. **51**(13), 3125–3129 (2012).
9. R. Liu, D. Tu, Y. Liu, H. Zhu, R. Li, W. Zheng, E. Ma, and X. Chen, "Controlled synthesis and optical spectroscopy of lanthanide-doped $KLaF_4$ nanocrystals," Nanoscale **4**(15), 4485–4491 (2012).
10. D. Chen, Y. Yu, F. Huang, P. Huang, A. Yang, and Y. Wang, "Modifying the size and shape of monodisperse bifunctional alkaline-earth fluoride nanocrystals through lanthanide doping," J. Am. Chem. Soc. **132**(29), 9976–9978 (2010).
11. F. Wang and X. Liu, "Recent advances in the chemistry of lanthanide-doped upconversion nanocrystals," Chem.

#252507 Received 22 Oct 2015; revised 21 Dec 2015; accepted 23 Dec 2015; published 8 Mar 2016

Soc. Rev. **38**(4), 976–989 (2009).
12. J. Shen, L. D. Sun, and C. H. Yan, "Luminescent rare earth nanomaterials for bioprobe applications," Dalton Trans. **24**(42), 5687–5697 (2008).
13. T. Nann, "Phase-transfer of CdSe@ZnS quantum dots using amphiphilic hyperbranched polyethylenimine," Chem. Commun. (Camb.) **13**(13), 1735–1736 (2005).
14. B. Ungun, R. K. Prud'homme, S. J. Budijon, J. Shan, S. F. Lim, Y. Ju, and R. Austin, "Nanofabricated upconversion nanoparticles for photodynamic therapy," Opt. Express **17**(1), 80–86 (2009).
15. M. Haase and H. Schäfer, "Upconverting nanoparticles," Angew. Chem. Int. Ed. Engl. **50**(26), 5808–5829 (2011).
16. G. Blasse and B. C. Grabmaier, *Luminescent Materials* (Springer, 1994).
17. F. Auzel, "Upconversion and anti-Stokes processes with *f* and *d* ions in solids," Chem. Rev. **104**(1), 139–174 (2004).
18. J. Zhao, D. Jin, E. P. Schartner, Y. Lu, Y. Liu, A. V. Zvyagin, L. Zhang, J. M. Dawes, P. Xi, J. A. Piper, E. M. Goldys, and T. M. Monro, "Single-nanocrystal sensitivity achieved by enhanced upconversion luminescence," Nat. Nanotechnol. **8**(10), 729–734 (2013).
19. Y. L. Wei, X. Y. Liu, X. N. Chi, R. F. Wei, and H. Guo, "Intense upconversion in novel transparent $NaLuF_4$:$Tb^{3+}$, $Yb^{3+}$ glass–ceramics," J. Alloys Compd. **578**, 385–388 (2013).
20. R. Dey, A. Pandey, and V. K. Rai, "$Er^{3+}$-$Yb^{3+}$ and $Eu^{3+}$-$Er^{3+}$-$Yb^{3+}$ codoped $Y_2O_3$ phosphors as optical heater," Sens. Actuators B Chem. **190**, 512–515 (2014).
21. D. Chen, Y. Chen, H. Lu, and Z. Ji, "A bifunctional Cr/Yb/Tm:$Ca_3Ga_2Ge_3O_{12}$ phosphor with near-infrared long-lasting phosphorescence and upconversion luminescence," Inorg. Chem. **53**(16), 8638–8645 (2014).
22. K. Z. Zheng, Z. Y. Liu, C. J. Lv, and W. P. Qin, "Temperature sensor based on the UV upconversion luminescence of $Gd^{3+}$ in $Yb^{3+}$-$Tm^{3+}$-$Gd^{3+}$ codoped $NaLuF_4$ microcrystals," J. Mater. Chem. C Mater. Opt. Electron. Devices **1**(35), 5502–5507 (2013).
23. D. Chen, L. Liu, P. Huang, M. Ding, J. Zhong, and Z. Ji, "$Nd^{3+}$-sensitized $Ho^{3+}$ single-band red upconversion luminescence in core–shell nanoarchitecture," J. Phys. Chem. Lett. **6**(14), 2833–2840 (2015).
24. D. Chen and Y. Wang, "Impurity doping: a novel strategy for controllable synthesis of functional lanthanide nanomaterials," Nanoscale **5**(11), 4621–4637 (2013).
25. F. Wang and X. Liu, "Upconversion multicolor fine-tuning: visible to near-infrared emission from lanthanide-doped $NaYF_4$ nanoparticles," J. Am. Chem. Soc. **130**(17), 5642–5643 (2008).
26. J. Wang, R. Deng, M. A. MacDonald, B. Chen, J. Yuan, F. Wang, D. Chi, T. S. Hor, P. Zhang, G. Liu, Y. Han, and X. Liu, "Enhancing multiphoton upconversion through energy clustering at sublattice level," Nat. Mater. **13**(2), 157–162 (2013).
27. G. Chen, T. Y. Ohulchanskyy, R. Kumar, H. Ågren, and P. N. Prasad, "Ultrasmall monodisperse $NaYF_4$:$Yb^{3+}$/$Tm^{3+}$ nanocrystals with enhanced near-infrared to near-infrared upconversion photoluminescence," ACS Nano **4**(6), 3163–3168 (2010).
28. T. Nann and P. Mulvaney, "Single quantum dots in spherical silica particles," Angew. Chem. Int. Ed. Engl. **43**(40), 5393–5396 (2004).
29. G. E. Arnaoutakis, J. Marques-Hueso, A. Ivaturi, K. W. Krämer, S. Fischer, J. C. Goldschmidt, and B. S. Richards, "Enhanced up-conversion for photovoltaics via concentrating integrated optics," Opt. Express **22**(5), A452–A464 (2014).
30. D. K. Yi, S. T. Selvan, S. S. Lee, G. C. Papaefthymiou, D. Kundaliya, and J. Y. Ying, "Silica-coated nanocomposites of magnetic nanoparticles and quantum dots," J. Am. Chem. Soc. **127**(14), 4990–4991 (2005).
31. D. Chen and P. Huang, "Highly intense upconversion luminescence in Yb/Er:NaGdF4@NaYF4 core-shell nanocrystals with complete shell enclosure of the core," Dalton Trans. **43**(29), 11299–11304 (2014).
32. T. J. Yoon, K. N. Yu, E. Kim, J. S. Kim, B. G. Kim, S. H. Yun, B. H. Sohn, M. H. Cho, J. K. Lee, and S. B. Park, "Specific targeting, cell sorting, and bioimaging with smart magnetic silica core-shell nanomaterials," Small **2**(2), 209–215 (2006).
33. R. D. Shannon, "Revised effective ionic radii and systematic studies of interatomic distances in halides and chalcogenides," Acta Crystallogr. A **32**(5), 751–767 (1976).
34. X. Liu, Y. Chi, G. Dong, E. Wu, Y. Qiao, H. Zeng, and J. Qiu, "Optical gain at 1550 nm from colloidal solution of Er3+-Yb3+ codoped NaYF4 nanocubes," Opt. Express **17**(7), 5885–5890 (2009).
35. H. Dong, L. D. Sun, and C. H. Yan, "Basic understanding of the lanthanide related upconversion emissions," Nanoscale **5**(13), 5703–5714 (2013).
36. V. D. Rodrı'quez, V. K. Tikhomirov, J. Me'ndez-Ramos, A. C. Yanes, and V. V. Moshchalkov, "Towards broad range and highly efficient down-conversion of solar spectrum by $Er^{3+}$-$Yb^{3+}$ co-doped nano-structured glass-ceramics," Sol. Energy Mater. Sol. Cells **94**(10), 1612–1617 (2010).
37. H. Guo, Z. Li, H. Qian, Y. Hu, and I. N. Muhammad, "Seed-mediated synthesis of NaY $F_4$:Y b, Er/$NaGdF_4$ nanocrystals with improved upconversion fluorescence and MR relaxivity," Nanotechnology **21**(12), 125602 (2010).
38. S. Zheng, W. Chen, D. Tan, J. Zhou, Q. Guo, W. Jiang, C. Xu, X. Liu, and J. Qiu, "Lanthanide-doped $NaGdF_4$ core-shell nanoparticles for non-contact self-referencing temperature sensors," Nanoscale **6**(11), 5675–5679 (2014).
39. D. L. Gao, X. Y. Zhang, H. R. Zheng, W. Gao, and E. J. He, "$Yb^{3+}$/$Er^{3+}$ codoped β-$NaYF_4$ microrods: Synthesis and tuning of multicolor upconversion," J. Alloys Compd. **554**(25), 395–399 (2013).

#252507 Received 22 Oct 2015; revised 21 Dec 2015; accepted 23 Dec 2015; published 8 Mar 2016

40. L. Jin, Y. N. Tan, Z. Quan, M. P. Li, and B. O. Guan, "Strain-insensitive temperature sensing with a dual polarization fiber grating laser," Opt. Express **20**(6), 6021–6028 (2012).
41. A. K. Soni, R. Dey, and V. K. Rai, "Stark sublevels in $Tm^{3+}$-$Yb^{3+}$ codoped $Na_2Y_2B_2O_7$ nanophosphor for multifunctional applications," RSC Advances **5**(44), 34999–35009 (2015).
42. A. K. Soni, R. Dey, and V. K. Rai, "Optical investigation in shuttle like $BaMoO_4$:$Er^{3+}$-$Yb^{3+}$ phosphor in display and temperature sensing," Sens. Actuators B Chem. **216**, 64–71 (2015).
43. V. K. Rai, "Temperature sensors and optical sensors," Appl. Phys. B **88**(2), 297–303 (2007).
44. W. Xu, X. Gao, L. Zheng, P. Wang, Z. Zhang, and W. Cao, "Optical thermometry through green upconversion emissions in $Er^{3+}$/$Yb^{3+}$-codoped $CaWO_4$ phosphor," Appl. Phys. Express **5**(7), 072201 (2012).
45. D. Chen, Z. Wan, Y. Zhou, X. Zhou, Y. Yu, J. Zhong, M. Ding, and Z. Ji, "Dual-phase glass ceramic: structure, dual-modal luminescence, and temperature sensing behaviors," ACS Appl. Mater. Interfaces **7**(34), 19484–19493 (2015).
46. R. Dey and V. K. Rai, "$Yb^{3+}$ sensitized $Er^{3+}$ doped $La_2O_3$ phosphor in temperature sensors and display devices," Dalton Trans. **43**(1), 111–118 (2014).

## 1. Introduction

In the past few decades, tomographic imaging techniques have played an important role in the investigation of novel biomedical imaging methods. It is due to their superiority in terms of unlimited penetration depth [1]. However, because of long image acquisition times they can't visualize real-time dynamics and have limited spatial resolution [2]. In comparison, photoluminescence (PL)-based biomedical imaging has the advantages of fast feedback, high sensitivity, and high resolution [3]. But it has a inevitable drawback, low tissue penetration depth. Optical probes that emit in the visible range (400-750nm) can only penetrate approximately 1 mm into the tissue because of the absorption and scattering of the photons [3,4]; for those emitting in the "biological transparency window", that is the first near-infrared (NIR-I) window (750-900 nm), the penetration depth only reaches several millimeters [5,6]. Thus, a new imaging method with high spatial resolution, fast feedback, and deep tissue penetration is desired to optimize the accuracy and sensitivity of biomedical imaging.

First of all, the most basic work is to realize high spatial resolution. Near-infrared contrast agents have generated particular interest in recent years due to their emission at longer wavelengths where scattering is reduced, and auto-fluorescence is weak [7–9]. These advantageous features enable imaging with increased signal-to-background ratio to greater depths within tissue and realize high spatial resolution imaging. Extending this principle, materials emitting even further into the infrared, in the so-called NIR II region (1100-1600 nm), such as quantum dots [10,11], carbon nanotubes [12], and rare-earth ions have recently gained attention due to their ability to provide signal from even deeper within scattering tissues [13, 14].

Compared with the previously reported handful of NIR II organic dyes and QDs, lanthanide-doped nanoparticles possess outstanding chemical and optical properties, including low cytotoxicity, high efficiency, low photo-bleaching, long luminescence and photochemical degradation [15, 16]. More importantly, they can emit UV and visible light after excitation by near-IR (NIR) light, through a process known as photon upconversion [17]. At the same time, because of the fast feedback and deep tissue penetration features, some efforts have been focused on the study of the temperature-dependent UC luminescence due to significant potential applications in temperature sensors, thermal imaging and cancer treatment as well as an optical heater [18–22]. These unique properties render lanthanide-doped nanoparticle particularly useful in bio-sensing and bio-imaging applications.

Lanthanide-doped nanoparticles may provide a much needed solution for the above-mentioned problems. Herein, we selected co-precipitation in a binary solvent mixture of oleic acid and 1-octadecene to synthesize the hexagonal-phase $NaYF_4$:$Yb^{3+}$, $Er^{3+}$ NPs which have been widely used as the most efficient NIR-to-visible upconversion (UC) luminescent and probe in bioscience [23, 24]. For the medical applications of this material, we exploited not only the function of dual-mode emission of β-$NaYF_4$: $Yb^{3+}$, $Er^{3+}$ NPs in the near infrared (NIR) and visible regions with single wavelength excitation at 980 nm, but also the function

#252507 Received 22 Oct 2015; revised 21 Dec 2015; accepted 23 Dec 2015; published 8 Mar 2016

of physiological temperature sensing with the luminescence of $Er^{3+}$ in the visible region. The obtained nanoparticle can be realized water-dispersible through surface coating with silica. Also, the strategy to design dual mode sensing and imaging composites may be extended to prepare multi-functional platforms for targeted multi-mode imaging of various biological systems.

## 2. Experimental

### *2.1 Materials*

$Y(CH_3CO_2)_3 \cdot xH_2O$, (99.9%), $Yb(CH_3CO_2)_3 \cdot 4H_2O$, (99.9%), $Er(CH_3CO_2)_3 \cdot xH_2O$, (99.9%), 1-octadecene (90%), oleic acid (90%), $H_5NO$, were all purchased from Sigma-Aldrich. $NH_4F$ (98%) and Polyvinylpyrrolidone (PVP-40) were obtained from Aladdin. NaOH (AR), methanol (AR), ethanol (AR), hydrochloric acid (AR), were supplied by Sinopharm Chemical Reagent Company. Ethyl silicate (AR) was purchased from Shanghai Chemical Reagent Purchase And Supply Wulian Chemical Factory.

All chemicals were used without further purification. Doubly distilled water was used in all experiments.

### *2.2 General procedure for the synthesis of core nanoparticles*

Hexagonal-phase $NaYF_4$: $Yb^{3+}$, $Er^{3+}$ nanoparticles were prepared using a modified version of the synthesis previously published by Liu et al [25–27]. All reactions were carried out in a 50 mL three-neck roundbottom flask. Briefly, 2mL water solution of Ln $(CH_3CO_2)_3$ (0.2 M, Ln = Y, Yb, and Er), oleic acid (3 mL) and 1-octadecene (7 mL) was added to a 50-mL flask. The mixture was heated at 150 °C for 30 min to remove the water content from the solution before cooling down to 50 °C. Shortly thereafter, 5 mL of methanol solution containing $NH_4F$ (1.60 mmol) and NaOH (1 mmol) was added and the resultant solution was stirred for 30 min. After the methanol was evaporated, the solution was heated to 290 °C under argon for 1.5 h and then cooled down to room temperature. The resulting nanoparticals were precipitated by addition of ethanol, collected by centrifugation at 6000 rpm for 5 min, washed with ethanol several times, and re-dispersed in 4 mL of cyclohexane or dried at 60 °C for 12 h.

### *2.3 General procedure for the synthesis of water-dispersible $NaYF_4$: $Yb^{3+}$, $Er^{3+}$ @ $SiO_2$ nanocomposite*

The 1 mL as-prepared oleic acid-capped nanoparticles were dispersed in a 2-mL HCl solution (0.1 M) and ultra sonicated for 10 min to remove the surface ligands. After the reaction, the nanoparticles were collected via centrifugation at 12000 rpm for 20 min, and further purified by adding an acidic ethanol solution (pH 4; prepared by adding 0.1 M HCl aqueous solution to absolute ethanol). The nanoparticles were washed with ethanol several times until transparent, and re-dispersed in 2 mL of ethanol. Typically, 0.2 g PVP was dissolved in 4 mL deionized water with magnetic stirring at room temperature for 0.5 h. Then 1 mL ligand-free nanoparticles was added to the mixture solution, and added 1 mL ammonium hydroxide solution after stirring for 4 h. Finally, 1 mL TEOS was added dropwise to the solution with stirring at room temperature for 12 h to obtain a homogeneous water-dispersible $NaYF_4$: $Yb^{3+}$, $Er^{3+}$ @ $SiO_2$ nanocomposite [28–30].

### *2.4 Characterization of NPs*

The X-ray diffraction (XRD) pattern of $Er^{3+}$-$Yb^{3+}$ codoped $NaYF_4$ was recorded using Bruker D8 Advance X-ray diffractometer with Cu-Kα (1.5405 Å) radiation within 10-80 ° range of 2θ. Scanning electron microscopy (SEM) was performed on a SU8010 FE-SEM scanning electron microscope (HITACHI, Japan) operated at 1.0 kV and the SEM image of the water-dispersible β-$NaYF_4$: 3 mol.% $Er^{3+}$, 20 mol.% $Yb^{3+}$ @ $SiO_2$was operated at 10.0 kV. The UC and NIR II spectra were obtained at room temperature by using a PL3-211-P spectrometer

#252507 Received 22 Oct 2015; revised 21 Dec 2015; accepted 23 Dec 2015; published 8 Mar 2016

(HORIBA JOBIN YVON, America). For UC and NIR II steady-state spectra investigation, a 980 nm continuous diode laser was used to pump the samples. The experimental setup for temperature sensing was a TAP-02 analyzer of high temperature fluorescence (ORIENT KOJI, China).

## 3. Results and discussion

### *3.1 Structure and morphology*

Figures 1(a-e) shows SEM images of $Er^{3+}$-$Yb^{3+}$ codoped $NaYF_4$. The concentration of $Er^{3+}$ ions in the codoped $NaYF_4$ is varied keeping $Yb^{3+}$ ions concentration fixed at 20 mol%. It can be seen that the nanoparticles displayed uniform spherical morphologies and narrow size distributions. The particle size distribution confirms that with the increase of erbium ion concentration, the concentrations of erbium ion in the codoped $NaYF_4$ is 0.5 mol.%, 1 mol.%, 2 mol.%, 3 mol.%, 10 mol.%, the average diameters are 35.5 nm, 30.0 nm, 29.0 nm, 27.0 nm, 25.5 nm, respectively. The diffraction peaks of all the nanoparticles [Fig. 1(f)] can be indexed as a pure hexagonal $NaYF_4$:$Yb^{3+}$, $Er^{3+}$ phase (PDF No.16-0334), which is contributing to the upconversion luminescence properties. With further increase in $Er^{3+}$ ion concentration, no extra diffraction peaks were observed. The well defined peaks indicate the high crystallinity of the synthesized nanoparticles. As shown in Fig. 1(f), the (110) and (101) peak shifts towards higher diffraction angles with the increase of erbium ion concentration. As a result of shrinkage in unit-cell volume owing to the substitution of $Y^{3+}$ ions by smaller $Yb^{3+}$ ions and $Er^{3+}$ in the host lattice [i.e. (r ($Yb^{3+}$ 0.868 Å) < r ($Er^{3+}$ 0.890 Å) < r ($Y^{3+}$ 0.900 Å)] [21, 32], implying that doping-introduced lattice shrinkage in Er-doped $NaYF_4$.. Importantly, we also observed that the diffraction peaks broaden with increasing $Er^{3+}$ dopant content, also indicating a reduction of the average crystallite size which is consistent with SEM images.

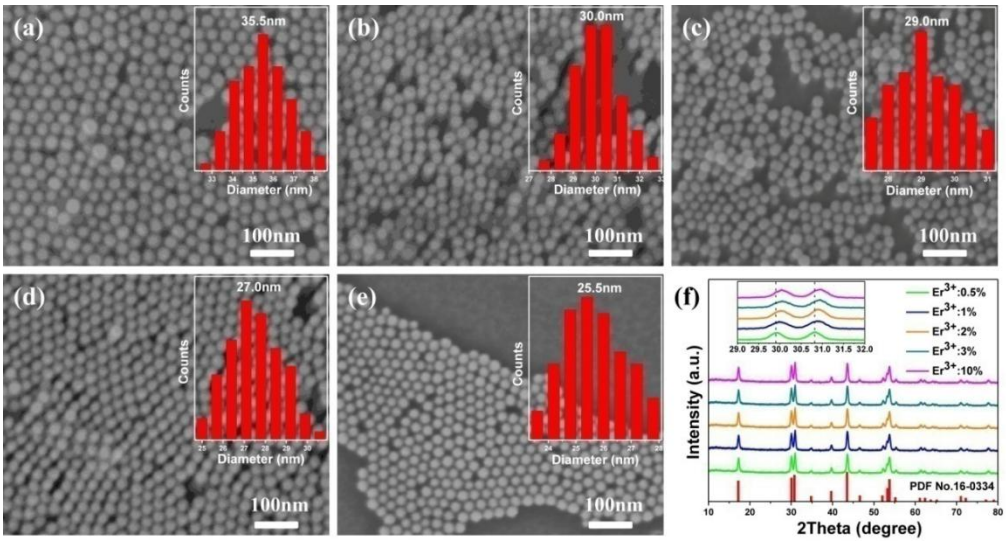


Fig. 1. (a-e) SEM images of β-$NaYF_4$: $Yb^{3+}$, $Er^{3+}$, the concentration of $Er^{3+}$ ion in the codoped $NaYF_4$ is 0.5 mol.%, 1 mol.%, 2 mol.%, 3 mol.%, 10 mol.%, respectively. The upper right inset is the corresponding particle size distribution. (f) The X-ray diffraction patterns of β-$NaYF_4$: $Yb^{3+}$, $Er^{3+}$; inset is the partially enlarged XRD pattern showing the shift of peaks.

### *3.2 Upconversion and Down-shifting study under 980 nm excitation*

Figure 2(a) shows the corresponding up-conversion luminescence spectra of $NaYF_4$ with different $Er^{3+}$/$Yb^{3+}$ ratio. The concentration of $Er^{3+}$ ions in the codoped $NaYF_4$ nanoparticles is varied keeping $Yb^{3+}$ ions concentration fixed at 20 mol.%. Under 980 nm laser excitation, green and red up-conversion emissions centered at around 521 nm, 541 nm, and 654 nm are

#252507 Received 22 Oct 2015; revised 21 Dec 2015; accepted 23 Dec 2015; published 8 Mar 2016

observed, corresponding to the $^2H_{11/2}\rightarrow{}^4I_{15/2}$, $^4S_{3/2}\rightarrow{}^4I_{15/2}$, $^4F_{9/2}\rightarrow{}^4I_{15/2}$ transitions of $Er^{3+}$ ions, respectively. Among these bands the intensity of green bands decreases more prominently while the intensity of red band decreases not significantly. It is due to the cross-relaxation processes ($^2I_{11/2}$/ $^4S_{3/2}$ + $^4I_{11/2}\rightarrow 2^4F_{9/2}$) as well as the non-radiative processes within the $Er^{3+}$ ions [33]. The intensity of all the UC emission peaks decreases with increasing the concentration of erbium ions up to 10 mol. %, the UC emission lifetime decreases with increasing the concentration of erbium ion, which is due to the concentration quenching. In order to understand the number of pump photons involved in the UC mechanisms the monolog plot of upconversion emission intensities, the excitation power-dependent UC emissions of 521, 541 and 654 nm were calculated. It is well known that the relation between the UCL intensity ($I_{UC}$) and the infrared excitation power ($P_{pump}$) can be expressed as [34, 35]

$$I_{UC} \propto \left(P_{pump}\right)^n \tag{1}$$

Where $n$ is the number of pump photons involved in the upconversion process. So, the slope of the straight line gives the $n$ value. Figure 2(b) is the log–log plot of UC emission intensity in β-$NaYF_4$: 3 mol.% $Er^{3+}$-20 mol.% $Yb^{3+}$ versus pump power, it is observed that the slopes corresponding to 521 nm, 541 nm and 654 nm emissions are ~1.78, ~1.63 and~1.74, respectively. The slopes of the linear fit of their emissions in the sample approach the integer 2, indicating that only a two-photon process is involved to produce the green and red emissions.

With the help of schematic energy level diagram [(Fig. 2(d)] the UC emissions in the green and red regions are due to the following mechanisms [36, 37]

1) $^4I_{15/2}$ + 980 nm (photon) $\rightarrow{}^4I_{11/2}$; $^4I_{11/2}$ + 980 nm (photon) $\rightarrow$ $^4F_{7/2}\rightarrow$ $^2H_{11/2}$, $^4S_{3/2}\rightarrow$ photon in the green region

2) $^4I_{11/2}\rightarrow$ $^4I_{13/2}$ + 980 nm (photon) $\rightarrow{}^4F_{9/2}\rightarrow$ photon in the red region and $^4I_{11/2}$ + $^4I_{13/2}\rightarrow{}^4F_{9/2}\rightarrow$ photon in the red region

It is worth mentioning that the slope of 654 nm (1.74) emission is larger than 541 nm (1.63), therefore, the UC emission in the red region is proposed mainly due to the process 2). In addition, the five samples not only exhibit obvious change of the relative intensities but also have different relative intensity ratios of red (600–700 nm) to emission green (500–600 nm) ($R_{R/G}$). $G$ is the integrated intensities corresponding to green bands and $R$ is the integrated intensities corresponding to red band. As can be seen from Fig. 2(c), the red/green ratio increases linearly with $Er^{3+}$ concentration. It should be noted that the ratio of the intensities of the red band and the green one is turned by the $Er^{3+}$ ions concentration; an increase in the content of $Er^{3+}$ ions induces a increase in $R_{R/G}$.

#252507 Received 22 Oct 2015; revised 21 Dec 2015; accepted 23 Dec 2015; published 8 Mar 2016

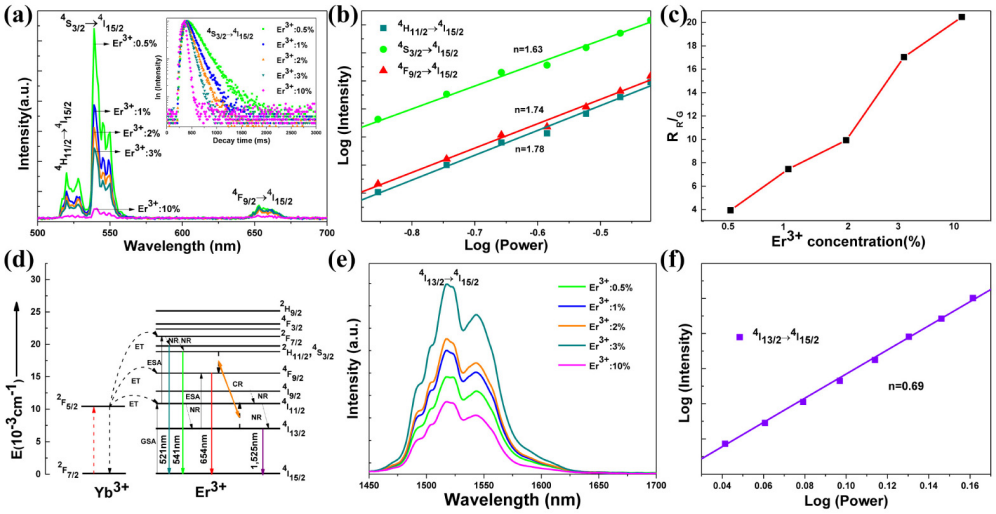


Fig. 2. (a) The UC emissions in β-$NaYF_4$: $Yb^{3+}$-$Er^{3+}$ crystals with different concentration of $Er^{3+}$ ions; (b)Log–log plot of UC emission intensity in β-$NaYF_4$: 3 mol.% $Er^{3+}$-20 mol.% $Yb^{3+}$ versus pump power ; (c) Calculated peak area ratio of the red region ($^4F_{9/2} \rightarrow {}^4I_{15/2}$) to the green region ($^2H_{11/2}$, $^4S_{3/2} \rightarrow {}^4I_{15/2}$); (d)Schematic energy level diagram for $Er^{3+}$-$Yb^{3+}$ energy transfer system under 980 nm excitation; (e) The SWIR emissions in β-$NaYF_4$: $Yb^{3+}$, $Er^{3+}$ crystals with different concentration of $Er^{3+}$ ions; (f) Log–log plot of DC emission intensity in β-$NaYF_4$: 3 mol.% $Er^{3+}$-20 mol.% $Yb^{3+}$ versus pump power.

Figure 2(e) shows the corresponding NIR II PL of $NaYF_4$ with different concentration of $Er^{3+}$ ions. In the down shifting emission spectrum bands around 1525 nm are observed [38]. The intensity of the short-wavelength infrared light increases with increasing the concentration of erbium ions up to 3 mol. %, but beyond this concentration of erbium ions it decreases due to concentration quenching. As shown in Fig. 2(f), the slope of the linear fit of 1525 nm emission in the sample is below 1, indicating that only a single-photon process is involved to produce the infrared emission.

Interestingly in the present case it is clearly observed that the intensities of upconversion emission peaks decrease when increasing the doping level of $Er^{3+}$ from 0.5 to 3 mol.%, however, the intensities of down shifting emission peaks increase substantially. It is plausible that the cross-relaxation process ($^4S_{3/2}$ + $^4I_{13/2} \rightarrow {}^4F_{9/2}$ + $^4I_{11/2}$) plays an important role in changing the $R_{R/G}$ [39]. An increase in the $Er^{3+}$ ion concentration enforces the $Er^{3+}$-$Er^{3+}$ interaction due to the shorter ion-ion distance leading to higher cross relaxation rates. The increased cross relaxation rates will cause a increase in the $R_{R/G}$ with the increase of $Er^{3+}$ ions which is in good agreement with the observation shown in the inset of Fig. 2(c) [40]. Figure 2(d) shows the simplified $Er^{3+}$-$Yb^{3+}$ energy level diagram of the 980 nm down shifting luminescence of the samples.

### *3.3 Study of temperature sensing behavior about β-$NaYF_4$: 20 mol. %$Yb^{3+}$, 3 mol. %$Er^{3+}$*

It is known that intensity-based measurements may suffer from variation of the sensor concentration and drifts of the optoelectronic system. Fluorescence ratio, however, is more reliable due to the freedom from these drawbacks. Different researchers have investigated the temperature sensing behavior for different rare earth doped materials by using the fluorescence intensity ratio (FIR) technique [31–43]. $Er^{3+}$ doped NPs can display a highly temperature-dependent emission, large Stokes' shifts and long lifetimes, which make such materials strong candidates for fluorescent sensing of the temperature [44–46]. In this work, depending on the temperature dependent physic-chemical property of the synthesized material the temperature sensing property has been studied, especially in the physiological range (25-

#252507 Received 22 Oct 2015; revised 21 Dec 2015; accepted 23 Dec 2015; published 8 Mar 2016

55 °C). Figure 3(a) represents the upconversion spectra of the optimal doping concentration 3 mol.% $Er^{3+}$ - 20 mol.% $Yb^{3+}$ codoped $NaYF_4$ under 980 nm excitation in the physiological range from 25 °C to 55 °C. The excitation intensity was well below 0.5 W/cm$^2$.

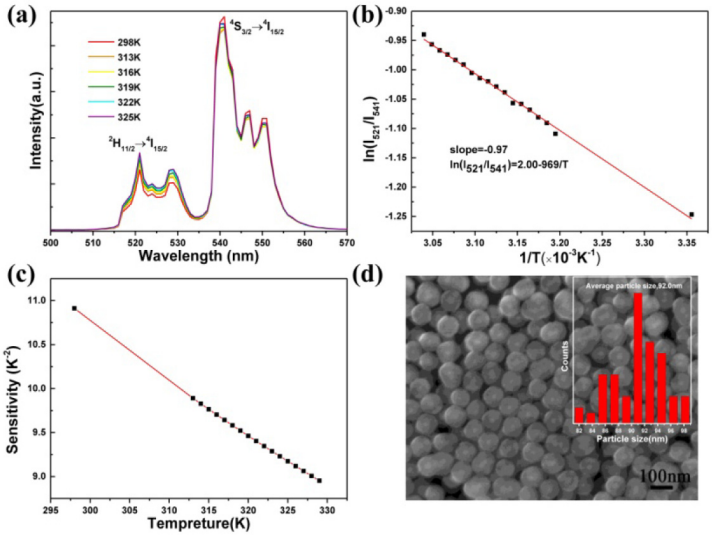


Fig. 3. (a) Upconversion emission spectra obtained at six different cuvette temperatures ($\lambda_{exc}$ = 980 nm); (b) The monolog plot of the FIR ($I_{521}/I_{541}$) as a function of inverse absolute temperature; (c) The sensitivity as a function of the absolute temperature; (d) SEM image of the water-dispersible β-$NaYF_4$: 3 mol.% $Er^{3+}$, 20 mol.% $Yb^{3+}$ @ $SiO_2$.

With the increasing of temperature, the FIR of 521 nm and 541 nm bands change due to the thermal population, while the all green emissions exhibit a little bit of quenching. The FIR varies according to the relation

$$\left(\frac{I_{521}}{I_{541}}\right) = C\exp\left(-\frac{\Delta E}{KT}\right) \tag{2}$$

Where $I_{521}$ and $I_{541}$ are the integrated intensities corresponding to green bands around 521 nm and 541 nm respectively. *C* is proportionality constant. *ΔE* is the energy difference between the thermally coupled levels $^4S_{3/2}$ and $^2H_{11/2}$, K = 0.695 K$^{-1}$ cm$^{-1}$ is the Boltzmann's constant. As the energy difference between $^2H_{11/2}$ and $^4S_{3/2}$ level is ~700cm$^{-1}$, thermal coupling is established between these levels. Figure 3(b) shows the monolog plot of FIR as a function of inverse absolute temperature. In accordance, with expression 1, a linear behavior is obtained; the best fit being Ln($I_{521}/I_{541}$) = 2.00 – 969 (1/T) (*T* given in K). This clearly demonstrates that the temperature can be accurately measured from the ratio of the 521 and 541 nm fluorescent intensities in the temperature range relevant for most biological systems. The linear fitting of the experimental data gives the slope value of about 969. This slope actually gives the *ΔE/K* value. From this value the calculated *ΔE* value comes out to be~674 cm$^{-1}$. This deviation of *ΔE* value from the actual value is small.

It is worthwhile to know the sensitivity (*S*) of the material and it is defined as the rate at which the FIR changes with temperature. Sensitivity can be defined as

$$S = \left(\frac{1}{FIR}\right)\left|\frac{d\left(FIR\right)}{dT}\right| \tag{3}$$

As the temperature rises from 25 °C to 55 °C, the sensitivity of the present material decreases. The maximum value of sensitivity is observed to be 0.1091 K$^{-1}$ at 298 K whereas

#252507 Received 22 Oct 2015; revised 21 Dec 2015; accepted 23 Dec 2015; published 8 Mar 2016

the minimum value of the sensitivity is 0.0895 $K^{-1}$ at 333 K. Figure 3(c) shows the sensitivity as a function of the absolute temperature, the sensitivity is higher than the reference which sensitivity is observed to be 0.0091$K^{-1}$ at 303 K temperature [46].

In order to satisfy biocompatibility of these UCNPs, we provide a simple and versatile protocol for hydrophilic modification of the as-synthesized nanoparticles through silica coating. The coating of silica arises from the hydrophobic interactions of the alkyl chains of silica with the octadecyl group of oleic acid on the surface of hydrophobic NPs. After hydrolysis and polycondensation of silanes, the hydrophilic silanol groups of silanes extend outwards, rendering NPs water soluble and allowing attachment of biomolecules. Figure 3(d) shows the SEM image of the water-dispersible $NaYF_4$: 3 mol. % $Er^{3+}$, 20 mol.% $Yb^{3+}$ @ $SiO_2$. The SEM images showed that there is a very uniform layer of silica on the $NaYF_4$: 3 mol.% $Er^{3+}$, 20 mol.% $Yb^{3+}$ nanoparticle; obviously, the average diameters is 92.0nm, the nanoparticles are monodisperse in water. Furthermore, the thickness of the silica shell was about 35 nm and could be adjusted by changing the amount of TEOS. In this way, multi-functional biological luminescent materials can be achieved.

## 4. Conclusions

In summary, the temperature sensing and dual-mode emission in the near infrared (NIR) and visible regions with single wavelength under 980 nm irradiation were achieved in β-$NaYF_4$: $Yb^{3+}$, $Er^{3+}$ nanoparticles. The efficient NIR II PL can be used for bioimaging and UC emission can be used for physiological temperature sensing. The FIR of the green bands corresponding to the $^2H_{11/2}\rightarrow {}^4I_{15/2}$ and $^4S_{3/2}\rightarrow {}^4I_{15/2}$ transition has been studied as a function of temperature to examine its temperature sensing behavior. In addition, we have shown that the obtained nanoparticles can be dispersed in water through use of a silica surface coating. This suggests that the strategy to design dual mode sensing and imaging composites may be extended to prepare multi-functional platforms for targeted multi-mode molecular imaging of various biological systems.

## Acknowledgment

The authors acknowledge financial support from Zhejiang Provincial Natural Science Foundation of China (No.LY14E020007&No.LR14E020003) and National Natural Science Foundation of China (No.11404311&No.51372235).

#252507 Received 22 Oct 2015; revised 21 Dec 2015; accepted 23 Dec 2015; published 8 Mar 2016